Radar Cross-Section of Potholes at Automotive Radar Frequencies

Abhilasha Srivastava†, Abhishek Goyal† and Shobha Sundar Ram
Indraprastha Institute of Information Technology Delhi, New Delhi 110020 India
E-mail: {abhilasha18152, abhishek18153, shobha}@iiitd.ac.in

***Abstract*—Automated detection of potholes in roads can increase driving safety for both passengers and vehicles. Potholes - especially those covered with water - are hard to detect using cameras, while vibration based detection using accelerometers cannot be used to find potholes ahead of the ego vehicle. In this paper, we study the feasibility of pothole detection using automotive radar by estimating and contrasting the pothole radar cross-section (RCS) with the backscatter from a flat road. We estimate the two-dimensional RCS of potholes from the scattered electric field simulated using finite difference time domain techniques. Our results show that the potholes give rise to significant backscatter only when the electrical properties of the pothole material are sufficiently different from the neighboring ground material. Alternatively, potholes with sloping walls forming a triangular cross-section give rise to stronger returns than those with a rectangular cross-section. The size, depth and curvature of the potholes give rise to only slight variations in the RCS. Also, the RCS from potholes filled with air and rainwater are comparable due to the low dielectric constant and conductivity of rainwater.**

***Index Terms*—automotive radar, millimeter wave, radar cross-section, potholes, FDTD**

I. Introduction

Undetected potholes and other defects on the road surface can significantly damage the lower bodies of vehicles especially the tires. In worst case scenarios, they can cause major accidents leading to road fatalities. Automated detection of potholes and road bumps is one of the objectives of advanced driver assistance systems (ADAS) that are currently being developed for improving driving conditions and reducing road fatalities. Currently, pothole detection is done manually. The process is time consuming, laborious and expensive. More recently, pothole detection has been investigated with different types of sensors including laser [1], [2], two-dimensional vision with cameras [3]–[5], three-dimensional vision based on stereo cameras [6], [7] and vibration sensing with accelerometers [8]. Each of the sensors have some limitations. Image data from cameras are not available during nights and under poor visibility conditions. Also, cameras cannot detect potholes when the ground is covered with water. In the case of stereo data, the problem becomes further complicated by the requirement of data association between corresponding views from two cameras especially since the views of road surfaces are usually blurry and grainy. Laser systems are expensive and not heavily used in most ADAS systems. Vibration data, on the other hand, are cheap to gather due to inexpensive accelerometer sensors. However, these sensors cannot be used to *look ahead* and warn the vehicle before it goes over the pothole on the road or detect a pothole in the neighboring lane of the vehicle. The objective of this paper is to assess the feasibility of using automotive radars for detecting potholes by estimating their scattering cross-sections and comparing these values with those of a flat ground without a pothole.

Automotive radars are being extensively used in ADAS systems for a variety of applications including pedestrian and vehicle detection, automatic cruise control, lane change assistance, rear and forward cross-traffic alerts and parking assistance [9]. The sensors are less expensive than lidars and cameras and are very good for precise range and velocity estimation of targets. There have been significant experimental studies to estimate the scattering from road surfaces at automotive radar frequencies [10]. However, there has been very limited work on the estimation of radar cross-section (RCS) of potholes. In [11], physics optics based models of a dielectric cylindrical structure were used to estimate the RCS of some types of road defects such as cracks and pebbles.

In this paper, we simulate a simple geometry of a pothole and estimate the monostatic RCS as a function of radar parameters such as radar frequency and aspect angle. We also study how the cross-section varies as a function of pothole parameters such as its shape, length, depth and the curvature of its walls. Finally, we study the variation of the pothole backscatter when it is filled with water when compared to the situation when the pothole is filled with air. We model the electromagnetic scattering of potholes using two-dimensional finite difference time domain (FDTD) techniques. FDTD is a full wave electromagnetic solver technique that models the complete scattering phenomenology - direct and multipath reflections and diffraction effects at edges. Usually, potholes are three dimensional structures with an elliptical cross-section. In this work, we consider a very simple two-dimensional pothole geometry shown in Fig.1a and study the effects of first order parameters such as the length, depth and material properties of pothole on its RCS. The pothole is recessed in a flat ground. For simplicity's sake, the pothole is assumed to be infinitely long along z axis. We consider a broad band plane wave excitation incident upon the pothole at an incident angle ϕ_i. Since, we are investigating

† A.S and A.G are joint first authors.

978-1-7281-6813-5/20/$31.00 ©2020 IEEE

look ahead systems, ϕ_i are greater than 90° (when the radar is directly above the pothole). We consider a Huygen's equivalent surface $\mathcal{S}$ at a small height above the ground level. Then, we estimate the magnetic current density on this surface based on field equivalence principles from the tangential electric field along the surface. The far field scattered field is computed from the magnetic current density from which the two-dimensional RCS of the pothole is estimated. Our results show that the RCS for air filled and rainwater filled potholes are comparable. Larger the dimensions of the pothole and larger curvatures in the walls of the pothole result in greater RCS. However, the RCS is most sensitive to the contrast in the dielectric properties of the material in the pothole to the material of the ground.

Our paper is organized as follows. In the following section, we describe the simulation method for generating the RCS of the potholes. In section III, we discuss the different pothole geometries under consideration, Finally, in section IV, we present the RCS of potholes as a function of different pothole and radar parameters. *Notation:* We have used the following notation in this work. Vectors are indicated with bold letters while other variables and constants are indicated with regular characters.

II. Derivation of RCS of Potholes from Simulation

We model the RCS of the pothole using finite difference time-domain (FDTD) equations on a two-dimensional simulation space, along the $x-y$ plane, as shown in Fig.1a. The simulation space spans $[L_x \times L_y]$m along the two axes.

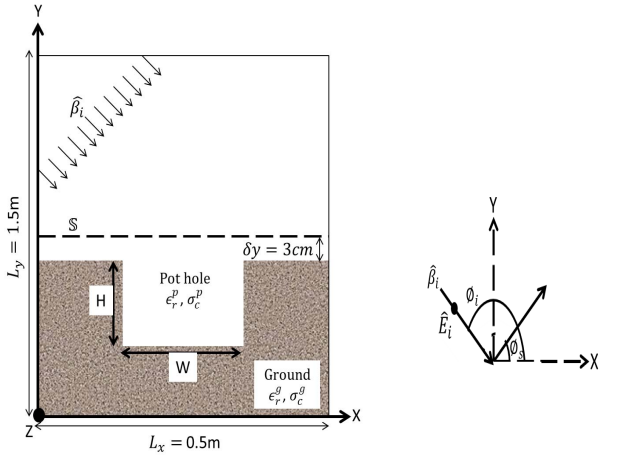

(a) (b)

Fig. 1: (a) Finite difference time domain simulation of two-dimensional pothole, of width W and depth H, with incident electric field along $\vec{\beta}_i$; (b) Incident electric field on pothole.

The pothole is assumed to be of finite width W along x, of depth H along y and infinite along the z direction. The pothole shown here has a rectangular shape. We have also considered a second type of pothole with a triangular shape (not shown here). The surface of the ground near the pothole is assumed to be flat and located at $y = 0$. The pothole is modeled as shown in Fig.1a with a dielectric constant of ϵ_r^p and a conductivity of σ_c^p while the ground is modeled with electrical parameters $(\epsilon_r^g, \sigma_c^g)$. The simulation space is discretised such that the grid resolution along x and y axes are equal to $\lambda_c/10$ where λ_c is the wavelength corresponding to the highest radar frequency (81GHz). The entire FDTD space is bounded by a perfectly matched layer of 0.02m thickness.

We simulate a plane wave horizontally polarized electric field incident at an angle ϕ_i with respect to the positive x axis as shown in Fig.1b. The source excitation for each line source is assumed to be a broadband signal of 4GHz bandwidth centered around a carrier frequency of 79GHz. The phasor incident electric field is represented by

$$\mathbf{E_i}(\lambda) = \hat{z} E_0(\lambda) e^{j\beta(x\cos\phi_i + y\sin\phi_i)}, \tag{1}$$

where $E_0(\lambda)$ is the amplitude of the field at λ wavelength and $\beta = \frac{2\pi}{\lambda}$ is the propagation constant with respect to free space. The plane wave is modeled by exciting multiple line sources, infinite along z axis along the plane normal to the wave propagation direction as shown in Fig.1b. All the source excitations are in phase. The incident electric field falls upon the pothole structure shown in the figure and gives rise to a reflected field $\mathbf{E_r}$ at every point in the simulation space. Therefore the total (phasor) electric field at any point in the simulation space is

$$\mathbf{E}(\lambda) = \mathbf{E_i}(\lambda) + \mathbf{E_r}(\lambda). \tag{2}$$

We consider a Huygen's surface $\mathcal{S}$ along the xz plane as shown. The surface spans $(x' \in [0, L_x], y' = \delta y', z' \in [-\infty, \infty])$ and is just slightly above $(\delta y' = 3cm)$ the pothole. Note that the extent of the Huygen's surface along x is greater than the width of the pothole and spans the entire FDTD simulation space along x. The time domain electric field at every point on the Huygen's surface $\mathcal{S}$ is Fourier transformed to obtain $\mathbf{E}(\lambda)$ for every λ.

On the basis of field equivalence principles, the magnetic current source on $\mathcal{S}$ can be computed from the total tangential electric field as

$$\mathbf{M_s} = 2\,\mathbf{E}(\lambda) \times \hat{y}|_{\mathcal{S}}. \tag{3}$$

We compute the magnetic current density $\mathbf{M_s}$ for every λ from the FDTD simulations. Then the electric vector potential $\mathbf{F}$ at any point in the far field (ρ, ϕ, z) is derived from the magnetic current source as

$$\mathbf{F} = \frac{\epsilon}{4\pi} \iint_{\mathcal{S}} \mathbf{M_s}(x', \delta y', z') \frac{e^{-j\beta R}}{R} ds', \tag{4}$$

where $R = \sqrt{(\rho - \rho')^2 + (z - z')^2}$ is the far-field distance from $\mathcal{S}$. Since this is a two-dimensional simulation, $\mathbf{M_s}$ does not change with respect to z' and (4) reduces to

$$\mathbf{F} = \frac{\epsilon}{4\pi} \int_{x'=0}^{L_x} \mathbf{M_s}(x') \left(\int_{z'=\infty}^{+\infty} \frac{e^{-j\beta\sqrt{(\rho-\rho')^2+(z-z')^2}}}{\sqrt{(\rho-\rho')^2+(z-z')^2}} dz' \right) dx'. \tag{5}$$

The inner integral (along z') in the above formulation reduces to the Hankel function $H_0^{(2)}(\beta|\rho - \rho'|)$ [12]. In far field conditions, at ϕ_s scattering angle, this function is approximately equal to

$$H_0^{(2)}(\beta|\rho - \rho'|) = \sqrt{\frac{2j}{\pi\beta}} \frac{e^{-j\beta\rho}}{\sqrt{\rho}} e^{+j\beta x' \cos\phi_s}. \quad (6)$$

The far field scattered electric field can be obtained from the electric vector potential by

$$\mathbf{E_s}(\lambda) = j\omega\eta(\hat{r} \times \mathbf{F}), \quad (7)$$

where ω is the angular frequency corresponding to λ and η is the impedance of free space. Substituting (5) and (6) in (7), we obtain the scattered electric field

$$\mathbf{E_s}(\lambda) = \hat{z} \sin\phi_s \left(\frac{e^{-j\beta\rho}}{\sqrt{\rho}}\right) \sqrt{\frac{j\beta}{2\pi}} \int_{x'=0}^{L_x} E(x') e^{j\beta x' \cos\phi_s} dx'. \quad (8)$$

Two-dimensional RCS for λ wavelength is defined as

$$\sigma_{2D}(\lambda) = \lim_{\rho\to\infty} \left[2\pi\rho \frac{|\mathbf{E_s}(\lambda)|^2}{|\mathbf{E_i}(\lambda)|^2}\right]. \quad (9)$$

Note that the unit of the RCS is meters and not meter-square. Therefore, the co-polarized two-dimensional cross-section of the pothole is

$$\sigma_{2D}^{HH}(\lambda) = \frac{\beta \sin^2\phi_s}{(E_0(\lambda))^2} \left| \int_{x'=0}^{L_x} E(x', \lambda) e^{j\beta x' \cos\phi_s} dx' \right|^2. \quad (10)$$

The monostatic cross-section can be estimated from $\phi_s = \phi_i$. In the discrete implementation of (10), we consider the x axis in the FDTD space that was discretised into N_x grids of size $\Delta x = \frac{L_x}{N_x}$. The two-dimensional RCS of the pothole is estimated from

$$\sigma_{2D}^{HH}(\lambda) = \frac{\beta \sin^2\phi_s L_x^2}{N_x^2 (E_0(\lambda))^2} \left| \sum_{n=0}^{N_x-1} E[n, \lambda] e^{j\beta n \Delta x \cos\phi_s} \right|^2. \quad (11)$$

III. Experimental Set Up

In the formulations described in the previous section there is no restriction on the shape of the pothole provided we correctly estimate the electric field along the Huygen's surface using the FDTD framework. In our work, we have studied the variation of the RCS as a function of radar parameters such as the monostatic aspect angle (ϕ_i) and the wavelength (λ). Since we are considering look-ahead systems, the pothole must be detected within a stopping distance of $d = 150m$. State-of-the-art millimeter wave radar sensors have very small antenna dimensions. For example, Continental's long range radar (ARS441) has an antenna of 83mm length resulting in a Fraunhofer far-field distance of 10.14m at 81 GHz. If the radar is mounted on the front bumper of the ego vehicle at an approximate height of $h = 0.6m$, then the angle of incidence will vary from $93.4°$ - when the car is 10.14 m from the the pothole - to $112°$ when the car is farthest from the pothole ($d = 150m$) as shown in Fig.2. We have also studied the effect of the pothole conditions on the RCS. Specifically, we have studied the effect of the length and the depth of the pothole, the curvature of the sides of the pothole and the electrical properties of the material inside the pothole. The curvature of the walls of the pothole are modeled by incorporating a slope in the walls as indicated by $\delta\theta$ shown in Fig.3a. In the extreme case, the walls slope significantly till we obtain a pothole of triangular shape. We consider two sizes of potholes - a large pothole of $H = 20cm$ and $W = 40cm$ and a small pothole of $H = 10cm$ and $W = 20cm$. For each of these cases, we have considered two types of ground or road conditions- a concrete road with high dielectric constant ($\epsilon_r^g = 10$) and an asphalt road with low dielectric constant ($\epsilon_r^g = 4$) [13]. Each pothole may be filled with air ($\epsilon_r^p = 1, \sigma_c^p = 0$) or rainwater ($\epsilon_r^p = 4.3$,$\sigma_c^p = 0.003 S/m$). Note that, depending on the salinity of the water, there can be considerable diversity in the electrical properties of water ranging from $\epsilon_r = 1$ to 81

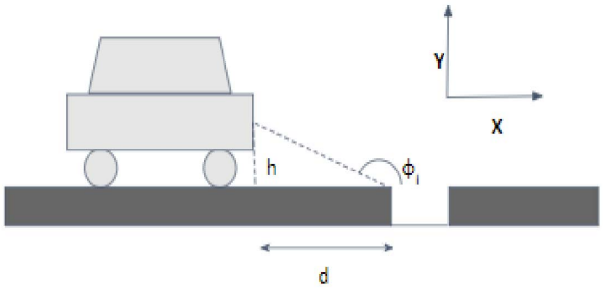

Fig. 2: Automotive radar mounted on a car at height $h = 0.6m$ looks ahead over distance d at pothole. Incident angle of radar to pothole is ϕ_i. As d varies from 150m to 10.14 m, ϕ_i changes from $112°$ to $93.4°$.

TABLE I: Radar and Pothole Parameters Considered in the Experimental Set Up

Parameters	Values
Radar center frequency	79 GHz
Radar Bandwidth	4 GHz
Aspect angle (ϕ_i)	$90°$ to $110°$
Pothole width (W)	0.2m or 0.4m
Pothole depth (H)	0.1m or 0.2m
Pothole curvature ($\delta\theta$)	$0°$ to $27°$
Ground dielectric constant (ϵ_r^g)	4 (Asphalt), 10 (Concrete)
Ground conductivity (σ_c^g)	0.006 S/m
Pothole dielectric constant (ϵ_r^p)	1 (Air), 4.3 (Rainwater)
Pothole conductivity (σ_c^p)	0 (Air), 0.003 (Rainwater)

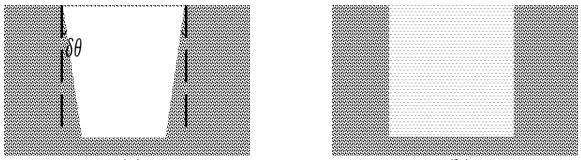

Fig. 3: Pothole configuration (a) with curvature along the side walls; (b) with rain water insider the aperture.

and from low to very high conductivity. The values chosen in this work, correspond specifically to rainwater at millimeter wave frequencies [13]. For each of these cases, we estimate the monostatic and bistatic RCS for different incident aspect angles. Table.I summarizes the radar and pothole parameters that we have studied in this work.

IV. Experimental Results

In this section, we present the estimated RCS for different types of potholes. Since the simulated RCS is two-dimensional, it is presented in units of meters ($dBmeters$ in log scale) instead of meter-square ($dBsm$ in log scale). In all of the cases, we have contrasted the results with those obtained from a flat ground without a pothole. This is to provide an indication of the feasibility of using radar backscatter as a feature for detecting the presence of potholes. Figure 4 shows the RCS for two types of potholes - those filled with rainwater and those filled with air for a fixed incident angle of $\phi_i = 105°$. Two different ground parameters are considered. In Fig.4a and 4c, the dielectric constant of the ground is $\epsilon_r^g = 10$ while in Fig.4b and Fig.4c, the dielectric constant is 4. The high dielectric constant pertains to roads made of concrete while the low dielectric constant corresponds to asphalt roads. We observe, in Fig.4a and 4c that the RCS of air filled pothole and water filled pothole are comparable across the frequency range from 77 to 81GHz. Interestingly, both the RCS values are significantly higher, by approximately 20dB, than the backscatter from a flat ground. This is because of the significant contrast in the dielectric constant of the pothole from the road. When we consider the same pothole dimensions but an asphalt road of $\epsilon_r^g = 4$, the RCS of both air-filled and water-filled potholes remain nearly the same as that of Fig.4a. The poor contrast between the pothole and the flat road backscatter indicate that the pothole will not be easy to detect for this type of road. Note that the dielectric constant for rainwater is around 4 which is almost identical to that of the road. From the four figures, we observe that there is a slight increase in the RCS as a function of the dimensions of the pothole. Finally, we present the RCS when the pothole is shaped like a triangle in Fig.4e. Interestingly, here we observe significant radar backscatter for both air and water filled potholes when compared to the flat road.

Next, we consider the variation of the RCS with the radar aspect angle in Fig.5. We consider aspect angle variation from $93.4°$ to $110°$. In this case, the pothole dimensions are large ($H = 20cm, W = 40cm$) and it is assumed to be filled with air and is recessed in a concrete ground. For greater aspect angles, the RCS falls slightly. The most significant fall in the RCS is observed at $\phi_i = 110°$.The aspect angle variation indirectly shows the effect of the radar's distance from the pothole since the distance is inversely proportional to the aspect angle as shown Fig.2.

Next, we plot the bistatic RCS of the pothole in Fig.6. The incident angle is fixed at $\phi_i = 105°$ and we have plotted the RCS for different values of ϕ_s for a fixed carrier frequency of 79.5GHz. Again, we have considered large air-filled pothole, in Fig.6a, and rainwater filled potholes, in Fig.6b, on the concrete road. The result in Fig.6a shows two prominent peaks - one at the specular reflection angle and one along the angle of incidence. The strength of the RCS along the specular angle is approximately 10dB higher than along the incident angle. In the case of Fig.6b, we observe multiple peaks. Fig.6c and Fig.6d show the RCS of a pothole with a triangular cross-section. Here, we observe stronger reflection at the monostatic angle rather than the specular angle for both air-filled and water filled potholes. Hence these potholes are the ones that are likely to be most easily detected by the radars.

Lastly, we consider the effect of the curvature of the walls of the pothole on the RCS in Fig.7. We previously mentioned that the triangular pothole has the maximum slope along the lateral walls. In this figure, we present the RCS as a function of smaller slopes from $\delta\theta = 0$ when the walls are completely straight to $\delta\theta = 27°$. For comparison purposes, we have also included the case of $\delta\theta = 90°$ where the ground is completely flat and there is no pot hole. We have again considered both air-filled (Fig.7a) and rainwater-filled (Fig.7b) potholes of large dimensions in a concrete ground. We observe that there is a slight reduction in the RCS with the increase in curvature. Again, we do not observe significant variation between the RCS of air-filled and rainwater-filled potholes.

V. Conclusion

We have estimated the two-dimensional RCS of potholes through simulations using FDTD techniques. We have compared the RCS of the potholes filled with air and rainwater with the backscatter from a flat road. Our results show that potholes give rise to significant backscatter when there is substantial variation in the electrical parameters of the pothole material with respect to the properties of the neighboring ground. Lower curvature of the walls and larger dimensions of the pothole cause a slight increase in the RCS values. Due to the low dielectric constant and conductivity of rainwater, there is not significant difference in the backscatter of air-filled potholes with respect to rainwater-filled potholes. Potholes with triangular cross-section give rise to much stronger backscatter than those with rectangular cross-sections and possibly the easiest to detect with look-ahead radar.

References

[1] K. Chang, J. Chang, and J. Liu, "Detection of pavement distresses using 3d laser scanning technology," in *Computing in civil engineering (2005)*, 2005, pp. 1–11.

[2] X. Yu and E. Salari, "Pavement pothole detection and severity measurement using laser imaging," in *2011 IEEE International Conference on Electro/Information Technology*. IEEE, 2011, pp. 1–5.

[3] J. Eriksson, L. Girod, B. Hull, R. Newton, S. Madden, and H. Balakrishnan, "The pothole patrol: using a mobile sensor network for road surface monitoring," in *Proceedings of the 6th international conference on Mobile systems, applications, and services*. ACM, 2008, pp. 29–39.

[4] C. Koch and I. Brilakis, "Pothole detection in asphalt pavement images," *Advanced Engineering Informatics*, vol. 25, no. 3, pp. 507–515, 2011.

[5] Y. Jo and S. Ryu, "Pothole detection system using a black-box camera," *Sensors*, vol. 15, no. 11, pp. 29 316–29 331, 2015.

[6] K. C. Wang, "Challenges and feasibility for comprehensive automated survey of pavement conditions," in *Applications of Advanced Technologies in Transportation Engineering (2004)*, 2004, pp. 531–536.

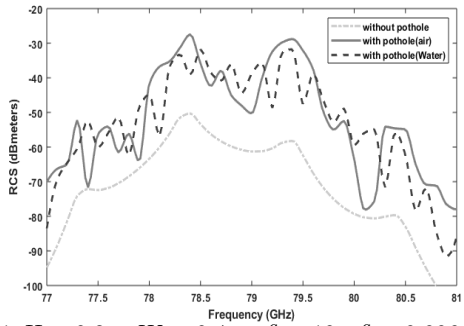

(a) $H = 0.2m, W = 0.4m, \epsilon_r^g = 10, \sigma_c^g = 0.006S/m$

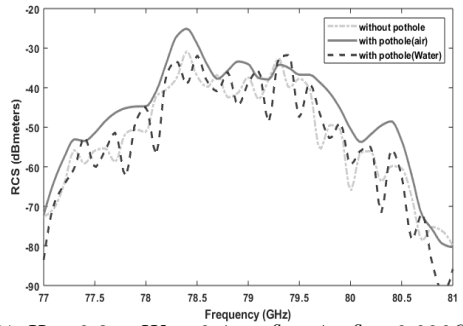

(b) $H = 0.2m, W = 0.4m, \epsilon_r^g = 4, \sigma_c^g = 0.006S/m$

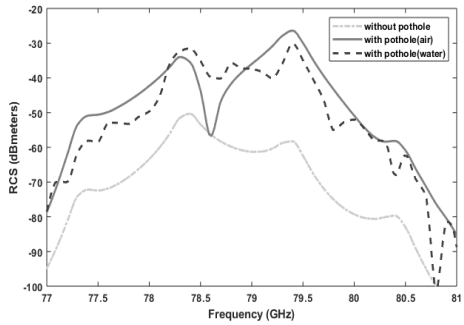

(c) $H = 0.1m, W = 0.2m, \epsilon_r^g = 10, \sigma_c^g = 0.006S/m$

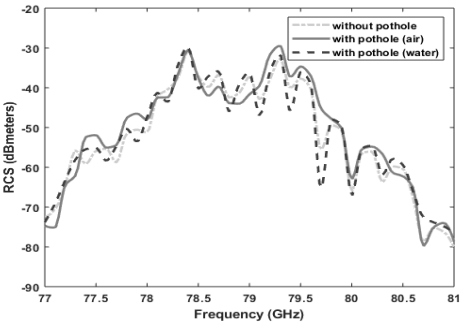

(d) $H = 0.1m, W = 0.2m, \epsilon_r^g = 4, \sigma_c^g = 0.006S/m$

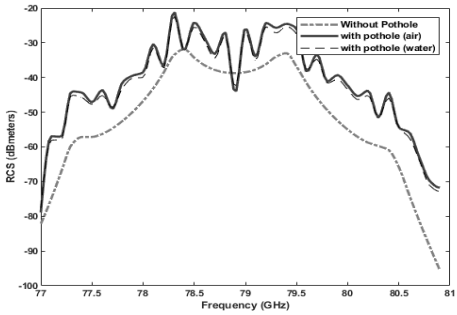

(e) $H = 0.2m, W = 0.4m, \epsilon_r^g = 4, \sigma_c^g = 0.006S/m$

Fig. 4: Monostatic radar cross-section of pothole of depth H and width W in the middle of a flat ground at incident angle $\phi_i = 105°$. Dielectric constant and conductivity of pothole are ϵ_r^p, σ_c^p and of ground are ϵ_r^g, σ_c^g. Two types of potholes are considered - pothole filled with air ($\epsilon_r^p = 1, \sigma_c^p = 0$) and pothole filled with water ($\epsilon_r^p = 4.3, \sigma_c^p = 0.003S/m$). The RCS of both cases are compared with that of a flat road without a pothole. (a-d) show the RCS of a pothole with a rectangular cross-section while (e) shows the RCS of a pothole with a triangular cross-section.

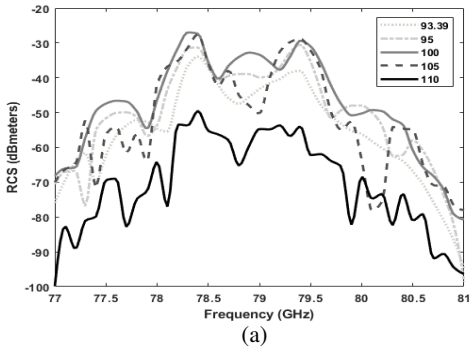

(a)

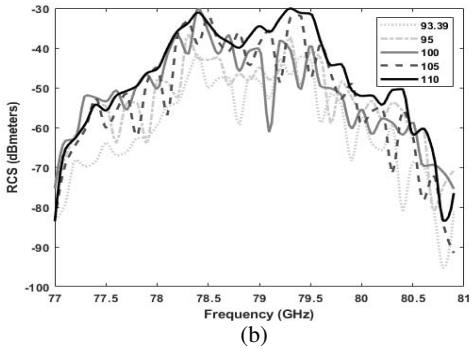

(b)

Fig. 5: Monostatic radar cross-section of (a) air-filled, (b) rainwater-filled pothole of depth $H = 0.2m$ and width $W = 0.4m$ in the middle of a flat concrete ground, of dielectric constant $\epsilon_r^g = 10$, at varying incident angle ϕ_i.

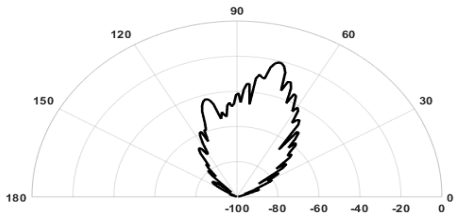

(a) $\phi_i = 105^\circ$, air-filled rectangular pothole

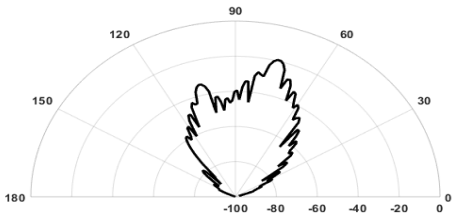

(b) $\phi_i = 105^\circ$, rainwater-filled rectangular pothole

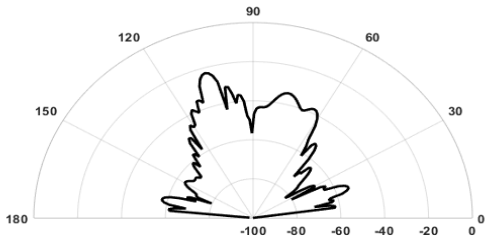

(c) $\phi_i = 105^\circ$, air-filled triangular pothole

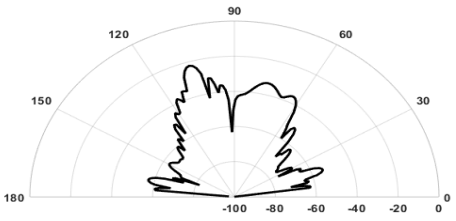

(d) $\phi_i = 105^\circ$, water-filled triangular pothole

Fig. 6: Bistatic radar cross-section of pothole, of depth $H = 0.2m$ and width $W = 0.4m$, in the middle of a flat concrete ground at incident angle ϕ_i and radar frequency of 79GHz.

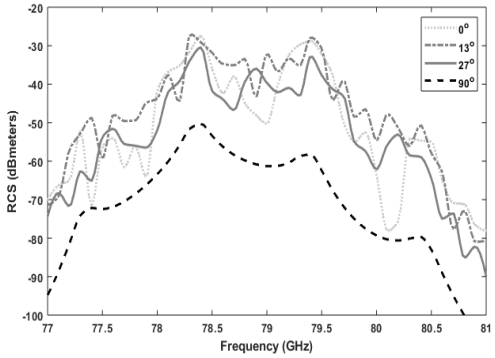

(a)

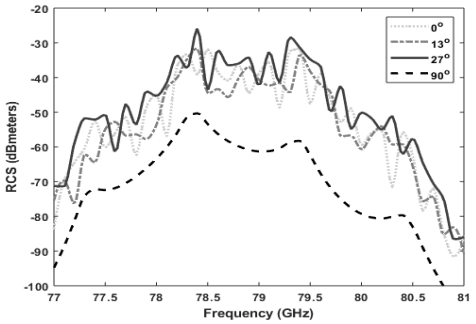

(b)

Fig. 7: Monostatic radar cross-section of (a) air-filled, (b) rainwater-filled pothole of depth $H = 0.2m$ and width $W = 0.4m$ in the middle of a flat concrete ground, of dielectric constant $\epsilon_r^g = 10$, at incident angle $\phi_i = 105^\circ$. Here the curvature of the walls is varied from $\delta\theta = 0$ to $\delta\theta = 90^\circ$.

[7] Z. Hou, K. C. Wang, and W. Gong, "Experimentation of 3d pavement imaging through stereovision," in *International Conference on Transportation Engineering 2007*, 2007, pp. 376–381.

[8] A. Mednis, G. Strazdins, R. Zviedris, G. Kanonirs, and L. Selavo, "Real time pothole detection using android smartphones with accelerometers," in *2011 International conference on distributed computing in sensor systems and workshops (DCOSS)*. IEEE, 2011, pp. 1–6.

[9] M. S. Greco, "Automotive radar," in *IEEE Radar Conference, Department of Information Engineering University of Pisa*, 2012, pp. 1–26.

[10] K. Sarabandi and E. S. Li, "Characterization of optimum polarization for multiple target discrimination using genetic algorithms," *IEEE Transactions on Antennas and Propagation*, vol. 45, no. 12, pp. 1810–1817, 1997.

[11] E. S. Li, "Physical optics models for the backscatter response of road-surface faults and roadside pebbles at millimeter-wave frequencies," *IEEE Transactions on Antennas and Propagation*, vol. 51, no. 10, pp. 2862–2868, Oct 2003.

[12] C. A. Balanis, *Advanced engineering electromagnetics*. John Wiley & Sons, 1999.

[13] T. Zhu, J. M. Carcione, and M. A. Botelho, "Reverse time imaging of ground-penetrating radar and sh-seismic data including the effects of wave lossq-compensated gpr imaging," *Geophysics*, vol. 81, no. 4, pp. H21–H32, 2016.